# Advances in Geo-Energy Research

### Original article

# Development of *in-situ* permeability testing system for low-permeability sandstone-type uranium deposits

Wei Wang<sup>1,2,3</sup>, Kun Yang<sup>1,2,3</sup>, Qinghe Niu<sup>1,2,3</sup>, Zeyu Han<sup>1,2,3</sup>, Junjian Zhang<sup>4</sup>, Vivek Agarwal<sup>5</sup>

#### **Keywords:**

In-situ test permeability pressure pulse method sandstone-type uranium deposits experimental model

#### Cited as:

Wang, W., Yang, K., Niu, Q., Han, Z., Zhang, J., Agarwal, V. Development of *in-situ* permeability testing system for low-permeability sandstone-type uranium deposits. Advances in Geo-Energy Research, 2025, 18(1): 69-83. https://doi.org/10.46690/ager.2025.10.06

#### Abstract

Rapid and accurate in-situ permeability testing is extremely important during the in-situ leaching of low-permeability sandstone-type uranium deposits. The current permeability testing methods rely on laboratory tests and the inversion of core or debris samples, which cannot reflect the true permeability of uranium deposits under their occurrence conditions. Therefore, this paper proposes a testing device based on the pressure pulse method for the in-situ permeability and corresponding automatic calculation software, and establishes the testing process. Specimen tests on a concrete model are carried out, and the testing results show consistency with the laboratory results and the micro-seepage numerical simulation results of uranium deposit cores in terms of magnitude and governing laws. However, due to factors such as the specimen tests not considering confining pressure, the uneven pouring, and the local cracking of the specimen caused by pulse pressure, the measured permeability deviation is between 7.14% and 21.47%. The permeability test results are related to the mineral stacking structure, the testing system, and the testing process. The permeability of uranium deposits with local gravel and basal cementation mode is relatively small. The main factors affecting the permeability test results are the deformation and friction of the high-pressure water storage tank and cable, the loose connection of various components, the integrity of the wellbore casing or the wellbore wall, and the installation position of the measuring section system. This study presents a rapid and accurate insitu permeability testing technology for low-permeability sandstone-type uranium deposits, providing technical support for site selection and effect prediction in in-situ learning.

#### 1. Introduction

Natural uranium, known as the "cornerstone of nuclear military industry and the granary of nuclear power", is an important strategic resource and energy mineral that guarantees national security (Mukherjee et al., 2023; Shannak et al., 2025). In China, there has been a low output and high demand for uranium resources for a long time, with

over 80% of uranium resources relying on imports and a persistently high external dependency (Chen et al., 2017; Fang et al., 2018). Thus, it is urgent to accelerate the development of uranium resources to ensure energy security. Sandstone-type uranium is the most important uranium resource in China (Akhtar et al., 2017), and its primary mining method is *in-situ* leaching (ISL) (Abzalov, 2012). Specifically, leaching agents

Yandy Scientific Press

\*Corresponding author.

E-mail address: wangweiuuu@163.com (W. Wang); yangkun\_upup@163.com (K. Yang); qinghniu@163.com (Q. Niu); 15103112094@163.com (Z. Han); junjianzhangcumt@126.com (J. Zhang); vivek.agarwal@northumbria.ac.uk (V. Agarwal). 2207-9963 © The Author(s) 2025.

<sup>&</sup>lt;sup>1</sup>Key Laboratory of Roads and Railway Engineering Safety Control (Shijiazhuang Tiedao University), Ministry of Education, Shijiazhuang 050043, P. R. China

<sup>&</sup>lt;sup>2</sup>Hebei Technology and Innovation Center on Safe and Efficient Mining of Metal Mines, Shijiazhuang 050043, P. R. China

<sup>&</sup>lt;sup>3</sup>School of Civil Engineering, Shijiazhuang Tiedao University, Shijiazhuang 050043, P. R. China

<sup>&</sup>lt;sup>4</sup>College of Earth Sciences & Engineering, Shandong University of Science and Technology, Qingdao 266590, P. R. China

<sup>&</sup>lt;sup>5</sup>College of Engineering and Environment, Northumbria University, Newcastle NE1 8ST, UK

| Testing method        |                            | Principle                              | Requirement                   | Application scope  | Advantages and drawbacks   | Reference   |
|-----------------------|----------------------------|--|-------------------------------|--|--|---|
|                       | Steady-state               | Darcy's law                            | Core sample                   | $\begin{array}{c} \text{Permeability} > \\ 10^{-18} \text{ m}^2 \end{array}$ | Low IR; moderate TS; long TT   | Stormont (1997);<br>Li et al. (2020)                                |
| Laboratory<br>testing | Transient                  | OUFT                                   | Core sample                   | Permeability: $10^{-21} \sim 10^{-16} \text{ m}^2$                           | Relatively high IR;<br>excellent TS;<br>relatively short TT                    | Marsala et al. (1998);<br>Cao (2017)                                |
|                       | Periodic oscillation       | OUFT                                   | Core sample                   | Permeability: $10^{-22} \sim 10^{-16} \text{ m}^2$                           | High IR; excellent TS; short TT  | Kranz et al. (1990);<br>Wang et al. (2015)                          |
|                       | Gas injection or degassing | OUFT                                   | Debris<br>sample              | 1  | Relatively short<br>TT; low TAC;<br>confining pressure<br>cannot be applied    | Egermann et al. (2005)  |
|                       | Experimental inversion     | Empirical<br>formula                   | Debris<br>sample              | 1  | Relatively long<br>TT; limited TAC;<br>confining pressure<br>cannot be applied | Gao and Hu (2013);<br>Jacob et al. (2021)                           |
| Field<br>testing      | Pumping test               | Dupuit formula<br>and Thiem<br>formula | <i>In-situ</i> rock formation | High-permeability formations   | Both the TE and TAC are low  | Mansur and Dietrich (1965);<br>Leven and Dietrich (2006)            |
|                       | Pressure pulse             | OUFT                                   | <i>In-situ</i> rock formation | Low-permeability formations  | Both the TE and TAC are high   | Bredehoeft and<br>Papadopulos (1980)                                |
|                       | Logging inversion          | Empirical formulas, etc.               | <i>In-situ</i> rock formation | 1  | Simple testing<br>method; limited<br>TAC                                       | Katsube and Hume (1987);<br>Li et al. (2011);<br>Long et al. (2025) |

**Table 1.** Comparison of commonly used permeability testing methods.

Notes: IR represents instrument requirements; TS represents testing stability; TT represents testing time; TAC represents testing accuracy; TE represents testing efficiency.

are injected into the uranium deposit through injection wells, which react with the uranium deposit to form uranium-bearing leachate that is then pumped to the surface through extraction wells for smelting and processing (Wang et al., 2022a). This technology boasts advantages such as simplicity, low infrastructure investment, low production cost, good environmental protection effect, and high resource utilization rate (Bowell et al., 2011; Niu et al., 2024a). Therefore, it has been widely applied in northern China, including the Yili basin, Tuha basin, Bayingobi basin, Ordos basin, Erlian basin, and Songliao basin (Su et al., 2020). However, the ISL technology has high requirements for the permeability of uranium deposits (Li and Yao, 2024; Liu et al., 2024b). It is generally believed that uranium deposits with a permeability coefficient greater than 0.1 m/d are suitable for ISL. Therefore, conducting rapid and accurate permeability testing of uranium deposits is a crucial step before ISL as well as a necessary means to pre-evaluate whether the uranium deposit can be extracted by ISL.

Scholars have proposed numerous methods over the last decades to test the permeability of rocks/rock masses, promoting the development of theories, instruments and technologies for permeability evaluation (Schembre and Kovscek, 2003; Metwally and Sondergeld, 2011; Niu et al., 2024b). The principles, applicable scopes, advantages, and disadvantages of current mainstream permeability testing methods are shown in Table 1. The application scenarios of permeability testing can be divided into laboratory testing and field testing. Laboratory testing mostly uses core samples (with diameters of 25, 38 and 50 mm) and crushed samples (Dong et al., 2020; Niu et al., 2021), with most experimental principles based on onedimensional unsteady flow theory (OUFT). Testing with core samples can apply confining pressure, axial pressure, pore pressure, and temperature, which can approximately simulate the in-situ occurrence conditions of the formation (Huang et al., 2025). However, testing with crushed samples cannot reproduce the influence of *in-situ* stress on permeability, therefore it has significant limitations.

Common laboratory tests include the steady-state method, transient method, periodic oscillation method, gas injection/degassing method, and experimental inversion methods (such as mercury intrusion porosimetry (MIP), computed tomography (CT), and scanning electron microscopy (SEM)). The steadystate method is mainly based on Darcy's law, which can realize the testing of gas permeability and liquid permeability and is widely used in laboratories. However, it is mainly applicable to relatively high-permeability cores (permeability  $> 10^{-18}$  m<sup>2</sup>). If the permeability of the core sample is low, it takes a long time to reach a stable state during the test, resulting in low testing efficiency and poor testing accuracy. To address this shortcoming, Johnson et al. (1966) used the transient method to test low-permeability rock formations, which calculates permeability by using the law of pressure attenuation over

time in the upstream of the core sample, with the lower limit of permeability testing reaching 10<sup>-21</sup> m<sup>2</sup>. Since it does not require a stable seepage of fluid in the core sample, the testing time is short and the accuracy is high, whereas it has high requirements for the precision of instruments. This method has been applied to laboratory permeability testing of rocks such as granite (Selvadurai et al., 2005), shale (Ling et al., 2013), and claystone (Giot et al., 2018). Meanwhile, Kranz et al. (1990) proposed the periodic oscillation method to test the permeability of low-permeability rock formations. This is similar to the transient method, except that the input dynamic pressure is sinusoidal. Permeability in this method is calculated through the amplitude ratio and phase delay of the sinusoidal pressure between the upstream and downstream. The lower limit of testing can reach  $10^{-22}$  m<sup>2</sup>, with the highest testing accuracy and the shortest testing time. However, this method has extremely high requirements for instrument performance, so its application range is relatively limited (Bernabé et al., 2006; Hasanov et al., 2020).

In addition, to solve the difficulty of obtaining cores from broken rock formations, the permeability of samples can be calculated by injecting gas into or degassing from a sealed pressure chamber containing debris samples (Fisher et al., 2017; Zhao et al., 2020), which also draw on the principle of the transient method. Some scholars have also inverted permeability based on empirical formulas using quantitative data of pore structures obtained from experiments such as MIP, CT and SEM (Jiang et al., 2024; Ni et al., 2021; Zhou et al., 2025). Limited by the size of samples used and the pressure/temperature conditions, the permeability obtained from laboratory tests often differs greatly from the permeability of the *in-situ* rock formation (Cosenza et al., 1999). Considering that rock formations contain more discontinuous structures, such as fractures, laboratory-tested permeability often underestimates the in-situ permeability. Therefore, it is extremely important to realize the permeability testing of rock formations under in-situ conditions (Meng et al., 2011; Zhao and Kang, 2021).

The most commonly used method in the in-situ testing of rock formation permeability is the pumping test, which measures the permeability coefficient of rock formations based on the Dupuit formula (Butler Jr, 1988) and the Thiem formula (Peyraube et al., 2023). This method is mostly applied in geological survey work to test shallow-buried soil layers or porous rock formations; however, the generally recommended testing time is more than ten days, resulting in low testing efficiency. For low-permeability or deep-buried rock formations, Bredehoeft and Papadopulos (1980) proposed an insitu permeability testing method based on the pressure pulse method. This method treats the rock formation as an infinite space and calculates permeability through changes in water injection pressure, which is somewhat different from the transient method used in laboratory tests. It has been applied in the evaluation of concrete permeability in underground compressed air energy storage projects (Kim et al., 2012). The permeability inversion method from logging results mainly relies on rock formation density, porosity, compressional and shear velocities, combined with empirical models, artificial intelligence methods, etc. (Tang and Cheng, 1996; Iturrarán-Viveros and Parra, 2014; Gao and Yu, 2024). The testing process is simple but the results depend on the rationality of the inversion method and the accuracy of logging data, leading to limited accuracy in permeability inversion (Elkatatny et al., 2018). Obviously, to quickly and accurately obtain the insitu permeability of low-permeability sandstone-type uranium deposits, the pressure pulse method is the most direct and effective approach (Cui et al., 2009; Liu et al., 2024a). However, although the pressure pulse method has relatively matured in laboratory permeability testing, its application in field testing remains insufficient. Furthermore, the in-situ permeability testing of deep, low-permeability sandstone-type uranium deposits presents significant challenges: Under deep well and highpressure pulse conditions, most existing tools are designed for oil and gas reservoirs or shallow geological settings, lacking specialized solutions tailored to uranium in-situ leaching conditions. Achieving and maintaining an effective packer set under deep well and high-pressure pulse conditions to ensure the normal operation of in-situ permeability testing systems also poses a considerable challenge. Furthermore, uranium deposits often feature burial depths of hundreds of meters and multi-layer superimposed distributions (Wang et al., 2023; Zhou et al., 2023). Currently, no corresponding testing equipment or technology exists for conducting in-situ permeability tests on low-permeability sandstone-type uranium deposits.

To address the need for evaluating the reservoir permeability of low-permeability sandstone-type uranium deposits before ISL, firstly, this paper proposes the pressure pulse method for *in-situ* permeability testing, and its basic principles are introduced. Secondly, an *in-situ* permeability testing device and corresponding software are developed, and a permeability testing scheme and application technology are established. Finally, model tests for the *in-situ* permeability testing of low-permeability sandstone-type uranium deposits are carried out, the results are verified by the laboratory tests and microseepage numerical simulation of uranium deposit cores, and the effectiveness of the testing system and potential error sources are analyzed. This research provides a novel technology for rapidly and accurately testing the in-situ permeability of low-permeability sandstone-type uranium deposits, facilitating site selection and effect prediction for ISL.

#### 2. Theory of in-situ permeability test

#### 2.1 Testing principle

When conducting *in-situ* permeability testing on rock formations using the pressure pulse method, the downstream of the testing system (the rock formation to be tested) should be treated as an infinite seepage boundary condition, and the following assumptions should be made:

- 1) The seepage of water in the rock formation satisfies Darcy's law;
- 2) The disturbance of the applied pulse pressure on the microstructure of rock formations is negligible;
- 3) The flow of water in rock formations has a one-

dimensional radial characteristic, i.e., the permeability of rock formations can remain consistent in all directions.

Under these assumptions, the one-dimensional unsteady flow differential equation for confined water in the rock formation can be expressed as follows (Vemuri and Dracup, 1967):

$$\frac{\partial^2 h}{\partial r^2} + \frac{1}{r} \frac{\partial h}{\partial r} = \frac{S}{T} \frac{\partial h}{\partial t} \tag{1}$$

where h represents the water head; t represents the test time; rrepresents the radial distance from the center of the wellbore; S represents the storage coefficient of the rock formation; T represents the transmissivity of the rock formation.

The initial condition of the water head in the rock formation is:

$$h(r,0) = 0 (2)$$

$$H(0) = H_0 \tag{3}$$

where h(r,0) represents the water head distribution at any position in the test section; H(0) represents the water head within the test system under initial conditions; and H0 represents the applied water head. Eq. (2) indicates that under the initial state, the water head remains constant at all positions in the test section, and Eq. (3) indicates that under the initial condition, the change in the water head in the wellbore is equal to H0. The boundary conditions of the water head in the rock formation are:

$$h(\infty, t) = 0 \tag{4}$$

$$h(r_w, t) = H(t) \tag{5}$$

where  $h(\infty,t)$  represents the water head at infinity for any given time;  $r_w$  represents the wellbore radius;  $h(r_w,t)$  represents the water head of the wellbore wall at any time; H(t)represents the water head in the test system at any time. Eq. (4) indicates that the water head at infinity remains constant and equal to zero at any given time, i.e., it is not affected by the instantaneous water injection, and Eq. (5) indicates that the water head at the wellbore wall is equal to the water head in the test system.

The boundary conditions of the water head in the wellbore are:

$$2\pi r_{w}T\frac{\partial h}{\partial r}(r_{w},t) = V_{w}C_{w}\rho_{w}g\frac{\partial H(t)}{\partial t}$$
(6)

where  $C_w$  represents the compressibility of water;  $\rho_w$  represents the density of water; g represents the gravitational acceleration;  $V_w$  represents the volume of water in the test system. Eq. (6) indicates that the flow rate of water flowing into the rock formation is equal to the rate of decrease in the volume of water in the wellbore. Herein, the volume changes caused by the expansion and contraction of other components in the test system are ignored, and only the volume change of water is considered.

By performing the Laplace transform on Eq. (1) to Eqs. (6) and (7) can be obtained:

$$\frac{H}{H_0} = \frac{8\alpha}{\pi^2} \int_0^\infty \frac{\exp\left(\frac{-\beta u^2}{\alpha}\right)}{uf(u,\alpha)} du$$
 (7)

Among them,

$$f(u,\alpha) = [uJ_0(u) - 2\alpha J_1(u)]^2 + [uY_0(u) + 2\alpha Y_1(u)]^2$$
 (8)

$$\alpha = \frac{\pi r_w^2 S}{V_w C_w \rho_w \varrho} \tag{9}$$

$$f(u,\alpha) = [uJ_0(u) - 2\alpha J_1(u)]^2 + [uY_0(u) + 2\alpha Y_1(u)]^2$$
(8)  

$$\alpha = \frac{\pi r_w^2 S}{V_w C_w \rho_w g}$$
(9)  

$$\beta = \frac{\pi Tt}{V_w C_w \rho_w g}$$
(10)

where  $J_0(u)$ ,  $J_1(u)$ ,  $Y_0(u)$ , and  $Y_1(u)$  are the 0<sup>th</sup>-order and 1<sup>st</sup>order Bessel functions of the first and second kinds, respectively; u denotes the independent variable. As explicitly stated by Cooper Jr et al. (1967),  $\alpha$  and  $\beta$  are intermediate variables used to solve Eq. (7). When the ratio of  $\beta/\alpha$  is small, the approximate expression of Eq. (7) is as follows:

$$\frac{H}{H_0} = e^{4\alpha\beta} \operatorname{erfc}\left(2\sqrt{\alpha\beta}\right) \tag{11}$$

where  $\operatorname{erfc}(x)$  is the complementary error function. At this point,  $H/H_0$  is no longer a function of  $\alpha$  and  $\beta$  but a function of the product of  $\alpha\beta$ . Moreover, when  $\alpha > 10$ , Eq. (11) can be used to approximate the permeability of the rock formation.

The processing method for the curve of water head variation with time changes depending on the value of  $\alpha$ . Calculations are performed according to the methods of Bredehoeft and Papadopulos (1980) under three scenarios:  $\alpha < 0.1, 0.1 \le$  $\alpha \le 10$ , and  $\alpha > 10$ . For example, when  $\alpha < 0.1$ , the  $\beta$  value is determined from the standard curve using the graphical method based on the standard curve defined by Eq. (7), and the corresponding t value is determined from the test time curve. On this basis, the transmissivity of the rock formation can be calculated as follows:

$$T = \frac{V_w C_w \rho_w g \beta}{\pi t}$$
 The permeability coefficient (K) is:

$$K = \frac{T}{I} \tag{13}$$

where l is the length of the test section.

The permeability (k) is expressed as:

$$k = \frac{K\mu}{\rho_w g} \eqno(14)$$
 where  $\mu$  stands for the viscosity coefficient of water.

#### 2.2 Testing device

The principal diagram of the proposed permeability test device for low-permeability sandstone-type uranium deposits is shown in Fig. 1. This test device consists of four parts: A pulse pressure application system, a control and monitoring system, a fixing and sealing system, and a measuring section system. The pulse pressure application system includes an electric water pump, a high-pressure water storage tank, and a pneumatic valve; the control and monitoring system includes a pressure sensor, a cable, a data recorder, and a computer; the fixing and sealing system includes a hydraulic anchor and two packers; and the measuring section system includes an electroplating screen pipe and a transmission cable.

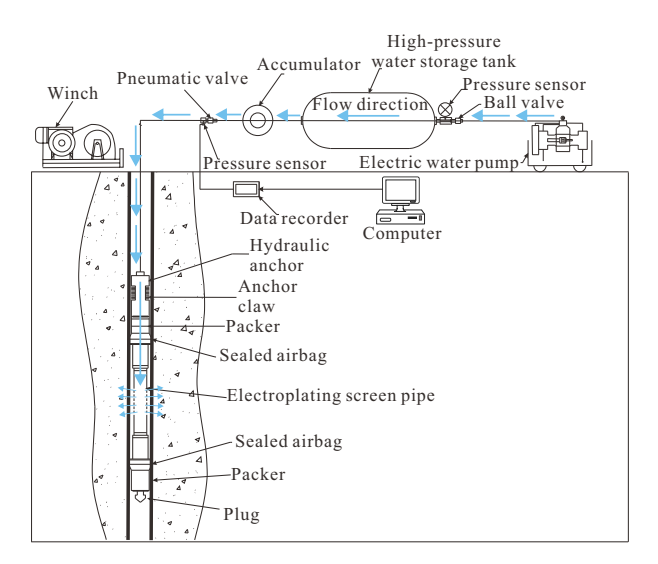


**Fig. 1**. Principle diagram of permeability test device for low-permeability sandstone-type uranium deposits.

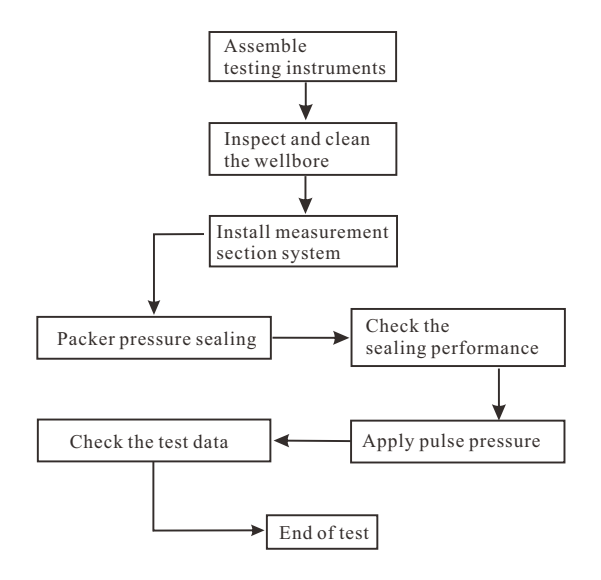


**Fig. 2**. Flowchart of *in-situ* permeability test for low-permeability sandstone-type uranium deposits.

The flow rate of the electric water pump is 4 L/min, and the volume of the high-pressure water storage tank is 0.5 m<sup>3</sup>. The water is injected into the packers and the measuring section system through two pipelines to provide setting pressure and pulse pressure, with a maximum design pressure of 10 MPa. The pneumatic valve can be opened instantly to ensure that the water in the high-pressure water storage tank can be quickly released. The diameter of the sealing pipeline and seepage pipeline used is 15 mm. The length of the pipeline can be increased or decreased according to the burial depth of the uranium deposit.

The pressure sensor outputs 4-20 mA transmitters with a measurement precision of  $\pm 0.1\%$ , which convert the measured pressure signal into an electrical signal and transmit it to the data recorder. The hydraulic anchor fixes the measuring section system to the measured uranium deposit layer in the wellbore by controlling the opening of the anchor claws. The packer

is made of rubber airbags, which are connected to the sealing pipeline and filled with water through a high-pressure water storage tank to expand and compress the wellbore for sealing. This component can withstand a maximum pressure of 10 MPa. The electroplating screen pipe is composed of a series of circular holes with a diameter of 15 mm, and its length can be adjusted to adapt to different thicknesses of target uranium deposit layers.

The entire device is lightweight and easy to operate. Its four parts can be disassembled and assembled at any time to adapt to the field conditions. Components such as pressure sensors, electric water pumps, high-pressure water storage tanks, and packers can all be adjusted and replaced according to the permeability of the rock formation and the diameter of the wellbore. The control and monitoring system can read data at any time and the permeability of the uranium deposit layer can be obtained through the developed permeability calculation software.

#### 2.3 Permeability calculation method

Eq. (7) is difficult to solve directly, hence it is mainly solved by the graphical method. Specifically, for different values of  $\alpha$ , the standard curve of  $H/H_0 - \beta$  can be obtained according to Eq. (7). For an  $\alpha$  value of 1, 0.8, 0.6, 0.4, 0.2,  $0.1, 0.08, 0.04, 0.01, 0.008, 0.004, 10^{-3}, 10^{-4}, \text{ and } 10^{-5}, \text{ the}$ obtained standard curves of  $H/H_0 - \beta$  can be obtained. The principle of permeability calculation is based on Section 2.1. To improve calculation efficiency, a permeability calculation software has been developed based on Python, which can automatically read the measured pulse pressure-time data and obtain the in-situ permeability of the tested rock formation through steps such as data interception, data fitting, curve matching, intersection marking, and permeability calculation. The x and y axis coordinate values corresponding to the intersection point are  $t_c$  and  $\beta_c$ , respectively, which are used to calculate the permeability.

The software's data fitting function first normalizes the pressure data by taking the logarithm of the time axis, then performs fitting using seventh-order polynomial least squares. The curve segment extraction function employs a Boolean index to retrieve and select curve data, enabling segment clipping. The curve matching function achieves alignment between extracted segments and standard curves through minimum mean square error calculation and horizontal coordinate translation. After identifying the best-matching standard curve and translation value, the intersection point is precisely pinpointed by locating where the experimental curve most closely approaches the standard curve.

#### 2.4 Testing steps

The flowchart of the *in-situ* permeability test for low-permeability sandstone-type uranium deposits is shown in Fig. 2. First, the four components are assembled, including the pulse pressure application system, control and monitoring system, fixing and sealing system, and measuring section system on the surface, and the firmness of the interfaces is carefully checked. Then, the wellbore is inspected and cleaned

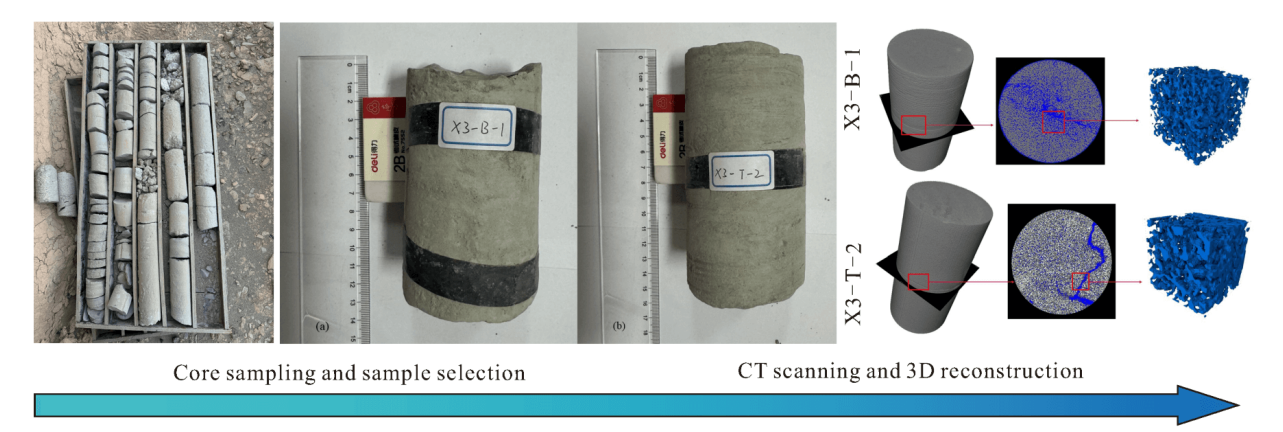


Fig. 3. Sample collection and the pore-fracture analysis process.

**Table 2**. Basic physical properties of the models.

| Model | Uniaxial<br>compressive<br>strength (MPa) | Elastic<br>modulus<br>(GPa) | Shear<br>modulus<br>(GPa) | Poisson's ratio (-) |
|-------|---|-----------------------------|---------------------------|---------------------|
| A     | 16.29                                     | 2.93                        | 1.19                      | 0.23                |
| В     | 8.92                                      | 2.11                        | 0.81                      | 0.31                |

using a downhole camera and well-flushing equipment, respectively, to remove cuttings and silt from the wellbore and ensure the integrity and flatness of the wellbore wall in the target interval to be tested. Next, the measuring section system is lowered to the target interval using a winch and fixed with a hydraulic anchor to ensure that the position of the measuring section system meets the requirements. After that, water is injected at 0.5 MPa into the two packers, and it is determined whether there is any leakage in the packers by observing the changes in pressure sensor data. If the sealing performance is good, water is injected at 10 MPa to seal the measuring section system. Finally, pulse pressure is applied through the control and monitoring system, the changing trend of pressure over time is recorded, and a preliminary check on the rationality of the data is conducted. If the requirements are met, the packers and hydraulic anchor are removed, the measuring section system is lifted to the surface, and the insitu permeability test is completed.

#### 3. Permeability testing of model specimens

## 3.1 Background of low-permeability sandstone-type uranium deposits

The engineering background of the experiment is based on the Shihongtan uranium deposit of the Tuha Basin in China, which belongs to a typical sandstone-type uranium deposit controlled by interlayer oxidation zones for mineralization. The southern zone of this deposit has a buried depth of 69.58-242.55 m, which can be divided into two ore bodies, located in the upper and lower sub-formations of the first lithological segment of the Xishanyao Formation within the Middle Jurassic System, respectively. The ore is mainly composed of loose to sub-loose conglomerates and medium coarse sandstones,

rich in organic matter and pyrite. The content of sand debris is high (>90%), while the amount of cement is low (<10%). The cement mainly consists of clay minerals, rock debris and a microdebris matrix. The pores in the ore are mainly intergranular dissolved pores and intragranular pores.

The permeability of the southern zone of the Shihongtan uranium deposit is generally poor, with an average permeability coefficient of 0.07 m/d. To further achieve ISL mining in this deposit, it is necessary to rapidly and accurately evaluate the permeability. In addition to conducting *in-situ* permeability tests, core samples at depths ranging from 170 to 190 m in the southern mining zone were gathered to analyze the micro pore-fracture structure characteristics by CT scanning and 3D reconstruction, simulate the micro seepage behavior, and verify the *in-situ* permeability test results (Fig. 3).

#### 3.2 Material proportioning

Considering to the mineral composition characteristics of low-permeability sandstone-type uranium deposits and the permeability differences of uranium deposits, two model specimens (hereinafter referred to as specimens) are designed to carry out model tests for permeability testing. The components of model A are cement, sand and gravel, with a material proportioning of 1:2:2 and a water-binder ratio of 0.7; the components of model B are cement and sand, with a material proportioning of 1:2 and a water-binder ratio of 0.5. The cement used is 42.5 ordinary Portland cement, and its main components are SiO<sub>2</sub>, FeO<sub>3</sub>, Al<sub>2</sub>O<sub>3</sub>, MgO, CaO, and SO<sub>3</sub>, accounting for 21.0%, 2.8%, 5.4%, 3.4%, 65.4% and 2.0% respectively.

The water used is ordinary tap water. The sand selected is natural river sand, with a particle size range of 0.5 to 1.0 mm, which serves as a fine aggregate with a fineness modulus of 3.2, a bulk density of 1,626 kg/m<sup>3</sup>, and an apparent density of 2,863 kg/m<sup>3</sup>. The gravel used is coarse aggregate, with a particle size of 5 to 10 mm. The basic physical properties of the two models are shown in Table 2.

#### 3.3 Model preparation

In order to verify the feasibility of the *in-situ* permeability testing system for low-permeability sandstone-type uranium

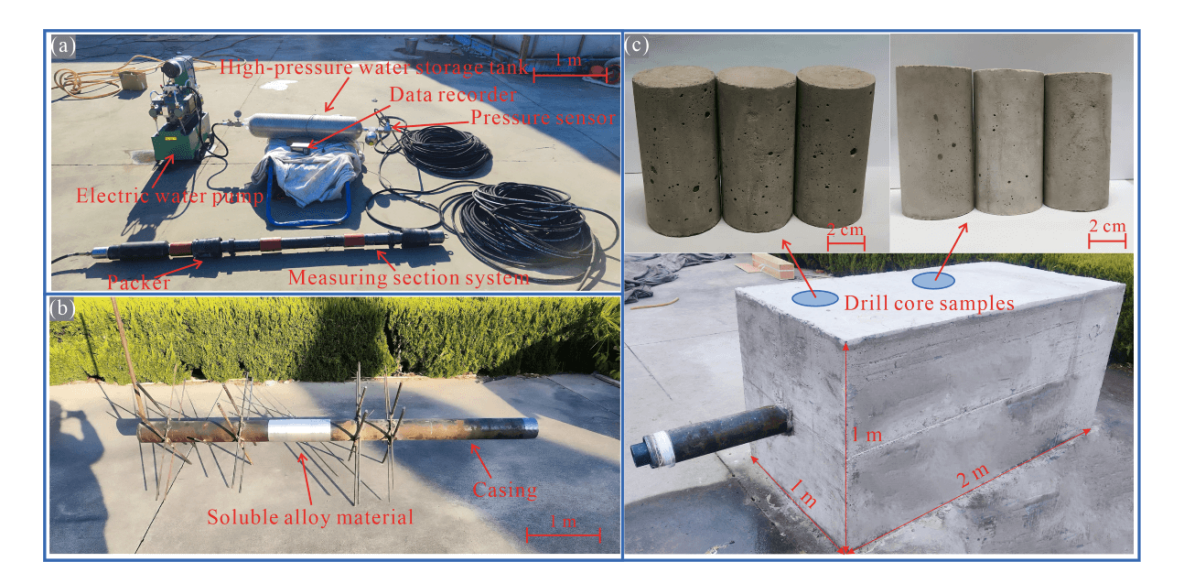


Fig. 4. Photograph of the prepared models and specimens.

deposits, model A and model B with dimensions of 1 m ×  $1 \text{ m} \times 2 \text{ m}$  are cast to carry out the model tests. During the casting process, a casing with an outer diameter of 122 mm and a length of 2 m is embedded, and a borehole with an inner diameter of 122 mm and a length of 1.5 m. The casing is connected by a soluble alloy material cylinder, which can melt when exposed to water, forming a bare wellbore wall for an *in-situ* permeability testing system. In the preparation process of the models, casting is conducted in layers with a thickness of 10 cm. Each layer is fully paved and then vibrated to be compact, ensuring the uniform mixing of materials. After the completion of casting, the models are cured for 14 days under a temperature of 20 °C and a relative humidity of 75%, thus forming the physical models for *in-situ* permeability testing, as shown in Fig. 4. After the *in-situ* permeability test is completed, a core sample with a diameter of 5 cm and a length of 10 cm is drilled from the models for indoor permeability testing to verify the accuracy of the in-situ permeability testing system.

#### 3.4 Testing scheme and data selection

In the test, the stepwise pressurized pulse method is adopted for permeability testing, i.e., the pulse pressure is gradually increased from 4 to 6 MPa at intervals of 0.5 MPa, so as to obtain the permeability of specimens under different pressures. After the pulse pressure is applied, it is necessary to demonstrate when to stop the test as the pressure decays. Since the pressure pulse method only focuses on the law of pressure decay rather than the actual measured pressure value, Bauer et al. (1995) believed that recording the pressure-time decay curve within a short period of time at the beginning of the test is sufficient for analyzing the permeability of rock mass. Furthermore, Chen et al. (2005) considered that the test requirements are met and the test can be terminated by using the pressure pulse method when the pressure drops to 80% of the initial value  $(H/H_0 = 0.8)$ , while for extremely dense rock formations, the permeability test time can be up to 30 minutes. Therefore, the pressure-time data when the pulse pressure decays to about 80% of the initial pressure is extracted to calculate the permeability of the model specimens in this work.

#### 3.5 Test results

Typical curves of the measured pulse pressure decay over time are shown in Fig. 5. After the pulsed water pressure is input into the model specimen, the water rapidly infiltrates into the pores from the wellbore wall, causing the pulse pressure to exhibit a pattern of "rapid decrease-slow decrease-stabilization". However, differences in the material proportions of the models result in significant permeability variations, which have a notable impact on the morphology of the pulse pressure curve. Specifically, the pulse pressure curve of model B decays faster and reaches equilibrium in a shorter time, which may indicate that model B has a greater permeability.

The relationship and fitting results between  $H/H_0$  and  $\log t$  are shown in Fig. 6. To apply the permeability calculation method described in Section 2.1, it is necessary to fit the obtained limited point data to generate a curve between  $H/H_0$  and  $\log t$  that matches the measured results. Polynomial functions are used for fitting all the measured data of the model specimens, and the resulting R<sup>2</sup> values are all greater than 0.999, confirming that the fitted equations can characterize the pulse pressure data of the specimens. Using the permeability calculation software developed in Section 2.3, the fitted equations are compared with the  $H/H_0 - \beta$ standard curves to identify the best-matching  $H/H_0 - \log t$  and  $H/H_0 - \beta$  curves (see Fig. 7). Then, the corresponding t and  $\beta$ values are obtained and substituted into Eqs. (12) and (13) to calculate the permeability test results of the model specimens, as shown in Table 3. In experiments and calculations, both model A and model B exhibit a  $C_w$  value of  $4.6 \times 10^{-10}$  m<sup>2</sup>/N and a  $V_w$  value of 0.062 m<sup>3</sup>.

The relationships between measured permeability of the model specimens and pulse pressure are shown in Fig. 8. As

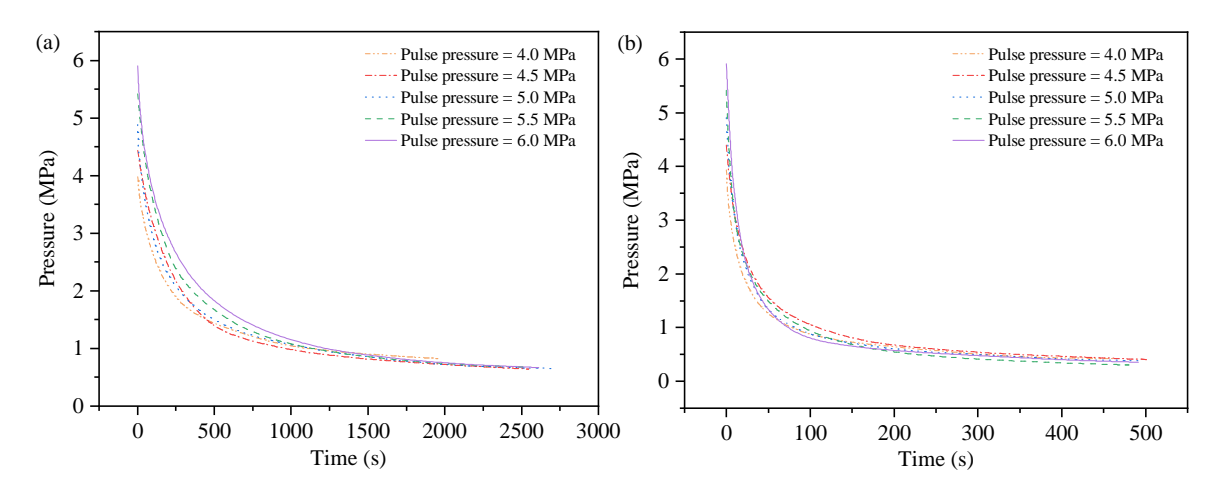


Fig. 5. Typical curves of measured pulse pressure decay over time: (a) Model A and (b) model B.

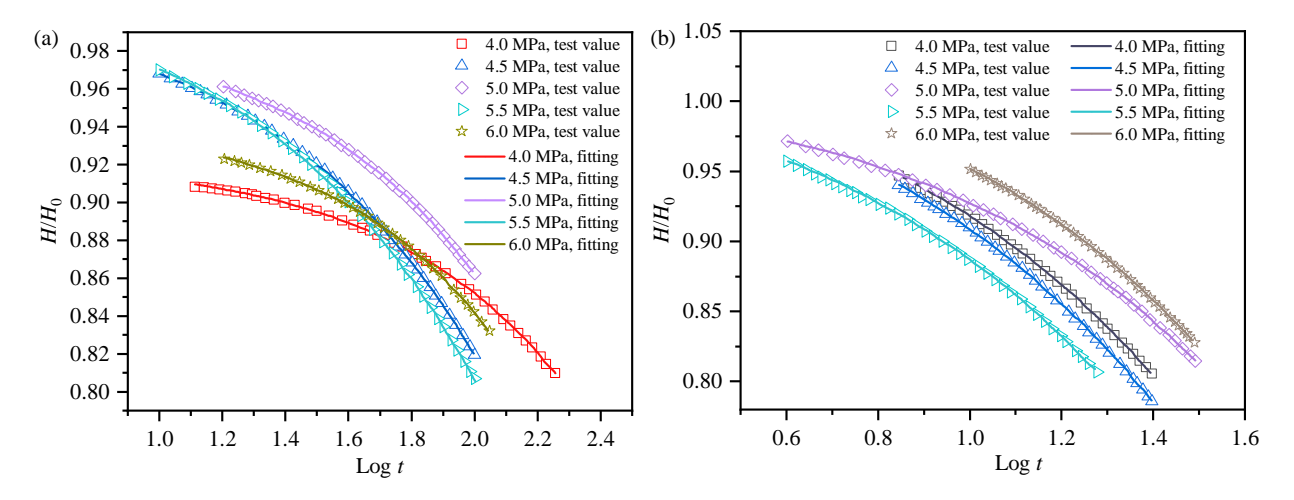


Fig. 6. Relationship and fitting results between  $H/H_0$  and  $\log t$ : (a) Model A and (b) model B.

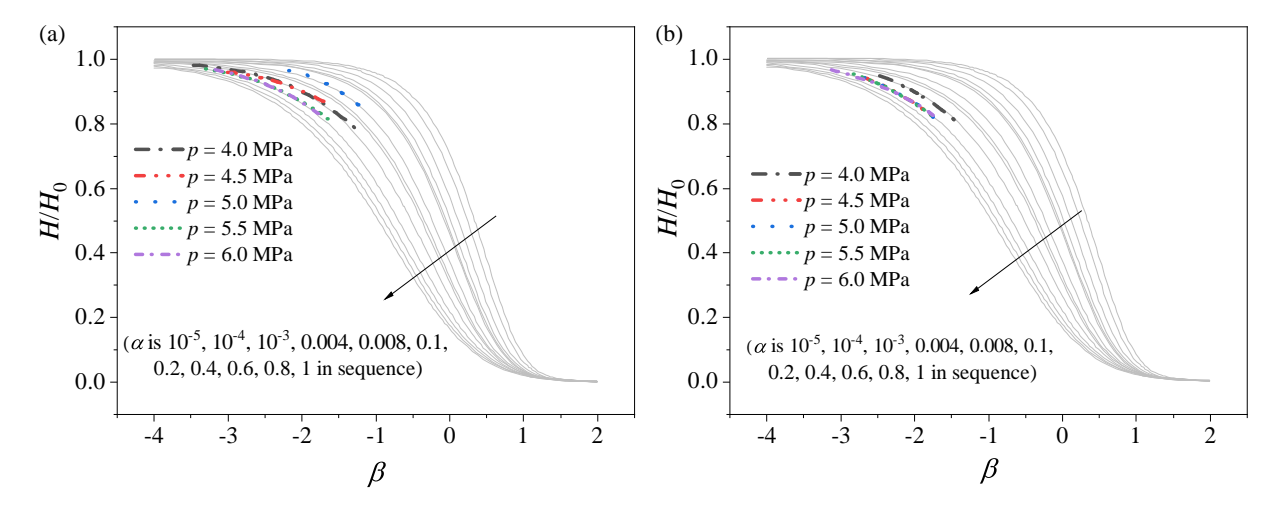
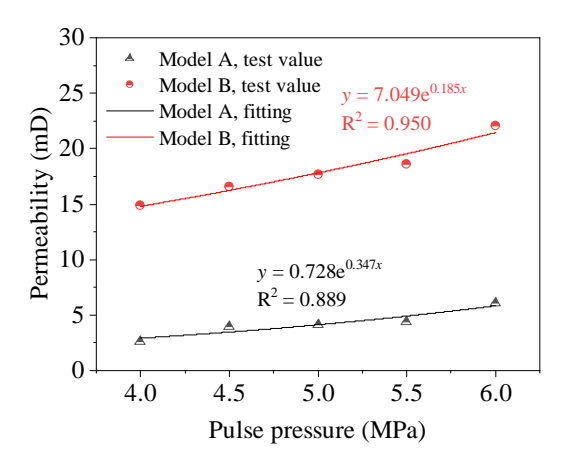


Fig. 7. Comparison between pulse pressure fitting curve and standard curve: (a) Model A and (b) model B.

| Model | <i>T</i> (°C) | $\mu (10^{-6} \text{ kPa·s})$ | P (MPa) | $t_c$ (s) | $\beta_c$ (-) | $K (10^{-11} \text{ m/s})$ | k (mD) |
|-------|---------------|-------------------------------|---------|-----------|---------------|----------------------------|--------|
|       | 5             | 1.5188                        | 4.0     | 104       | 0.03949       | 1.691                      | 2.655  |
|       | 5             | 1.5188                        | 4.5     | 69        | 0.03950       | 2.549                      | 4.003  |
| A     | 5             | 1.5188                        | 5.0     | 67        | 0.03956       | 2.629                      | 4.126  |
|       | 5             | 1.5188                        | 5.5     | 63        | 0.03970       | 2.806                      | 4.406  |
|       | 5             | 1.5188                        | 6.0     | 46        | 0.04000       | 3.872                      | 6.080  |
|       | 6             | 1.4728                        | 4.0     | 18        | 0.03956       | 9.787                      | 14.904 |
|       | 6             | 1.4728                        | 4.5     | 17        | 0.04033       | 10.562                     | 16.589 |
| В     | 6             | 1.4728                        | 5.0     | 15        | 0.03914       | 11.62                      | 17.691 |
|       | 5             | 1.5188                        | 5.5     | 15        | 0.03992       | 11.85                      | 18.611 |
|       | 5             | 1.5188                        | 6.0     | 12        | 0.03791       | 14.07                      | 22.080 |

**Table 3**. Model specimen permeability test results.



**Fig. 8**. Relationships between the measured permeability of the model specimen and pulse pressure.

the pulse pressure increases, the permeability of the model specimens shows an exponential growth trend, which indicates that pulse pressure has a relatively significant impact on permeability. This is because after water with high pulse pressure infiltrates into the specimen, it reduces the effective stress of the matrix therein, causing the expansion of pores and subsequent permeability improvement. The exponential increase in permeability with pulse pressure can be attributed to the reduction in effective stress within the rock matrix, a well-documented phenomenon in rock mechanics (Bernabe et al., 1982). When high pulse pressures are applied, the increase in pore fluid pressure counteracts the confining pressure acting on the rock skeleton. According to the principle of effective stress (Biot, 1941), this reduction in effective stress induces the elastic expansion of existing pores and microfractures, thereby enhancing the permeability of the rock matrix (David et al., 1994; Al-Wardy and , 2004). This mechanism is particularly pronounced in fractured or low-permeability rocks, as their pore connectivity is highly sensitive to stress variations. In addition, to ensure that the pressure sensor can accurately capture the attenuation law of pulse pressure and achieve the goal of reflecting the real permeability of the uranium, it is

crucial to select an appropriate pulse pressure.

## 4. Analysis and discussion of permeability test results

## **4.1** Verification by laboratory permeability testing

## 4.1.1 Permeability comparison of laboratory and model test

In order to verify the accuracy of the model test results obtained by the *in-situ* testing system for permeability using the transient pressure pulse method, cores with a diameter of 50 mm and a length of 100 mm were drilled from the prepared model. Laboratory permeability tests are carried out under a confining pressure of 8 MPa, during which the pore pressure is consistent with the pulse pressure in the model test. The permeability in the laboratory test is measured using the steady-state method based on Darcy's law, and the calculation formula is as follows (Ren et al., 2022; Kozhevnikov et al., 2024):

$$Q = -\frac{kA}{\mu} \frac{\Delta p}{L} \tag{15}$$

where Q represents the flow rate of water; A represents the cross-sectional area of sample;  $\Delta p$  represents the pressure difference between the upstream and downstream of the sample;  $\mu$  represents the water viscosity, and L denotes the length of the sample in the flow direction. The negative sign represents that water flows from the high-pressure side to the low-pressure side.

The laboratory permeability test results of core samples are shown in Fig. 9. The core permeability of model A ranges from 2.37 to 4.14 mD, and that of model B ranges from 13.84 to 17.50 mD. The laboratory test results of model A and model B are 7.07%-31.91% and 7.14%-20.74% lower than the model test results, respectively. The permeability measured by the model test is greater than that by the laboratory core test for the following reasons:

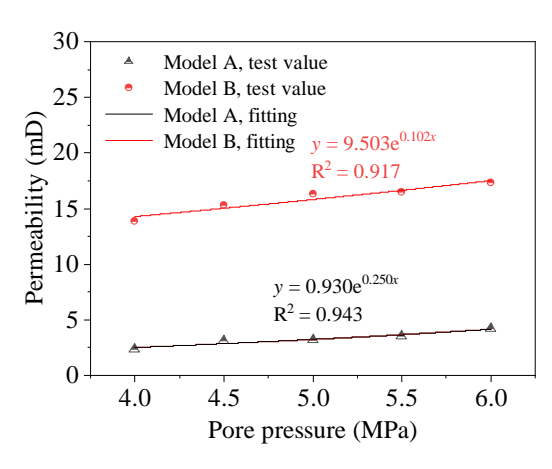


Fig. 9. Laboratory permeability test results of core samples.

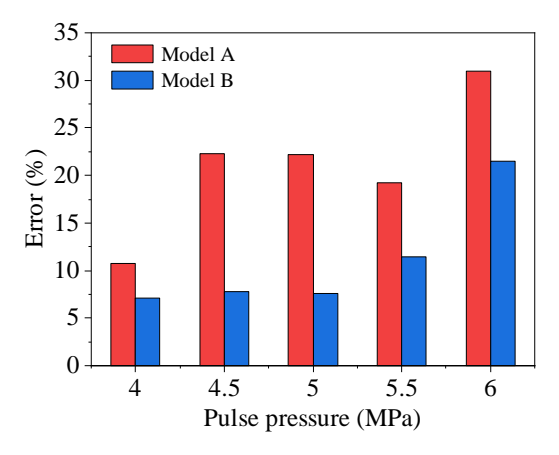


Fig. 10. Error analysis of laboratory permeability and model test permeability.

- The laboratory core test is carried out under the constraint of confining pressure, while the model boundary in the model test is a free interface, which leads to the compression of pores inside the core to a certain extent, resulting in a decrease in permeability;
- Although the model block material has been stirred as uniformly as possible during the pouring process, the large size of the model may still have some primary discontinuous surfaces (such as fractures), which leads to higher permeability;
- During the permeability test, the model specimen may crack under the action of pulse pressure, which increases the seepage channels of fluid and thus increases the permeability.

The core permeability increases with increasing pore pressure, which also conforms to the exponential function relationship, consistent with the fitting method of the model test. The law and order of magnitude of the laboratory test results are basically consistent with those of the model test results, which confirms the feasibility and reliability of the permeability testing system developed in this work, and it can be applied to the *in-situ* permeability testing of low-permeability sandstone-type uranium deposits.

**Table 4.** Average values of pore-fracture structure parameters for different samples.

| No.    | Length (µm) | Width<br>(µm) | Surface<br>area<br>(µm²) | Volume<br>(μm <sup>3</sup> ) | Shape factor (-) |
|--------|-------------|---------------|--------------------------|------------------------------|------------------|
| X3-B-1 | 169.25      | 93.89         | 55,442.90                | 1,424,622.24                 | 1.20             |
| X3-T-2 | 181.14      | 100.03        | 63,397.56                | 2,036,270.36                 | 1.23             |

#### 4.1.2 Error analysis

The error analysis of laboratory permeability and model test permeability is shown in Fig. 10. The error between the laboratory permeability and the model test permeability for model A ranges from 10.73% to 30.92%, and for model B, it ranges from 7.14% to 21.47%. On the whole, the error in permeability increases with the increase in pulse pressure. Excessive pulse pressure can expand the internal microstructure of the model and even lead to local cracking, causing the permeability to deviate from the actual value. The extent of this differs between the laboratory test and the model test, which is the main reason for the significant difference between the two models.

#### 4.2 Verification by numerical simulation

The layer-by-layer surface porosity analysis of samples is shown in Fig. 11. The surface porosities of sample X3-B-1 and sample X3-T-2 are 0.07%-1.39% and 0.50%-15.60%, with the average values of 0.55% and 1.95%.

The shape and distribution of micropores and fractures in sandstone samples are key factors determining their permeability behavior (Chi et al., 2025). To quantitatively characterize the microstructure of core samples, referring to previous literature (Niu et al., 2024b; Li et al., 2025), the pore and fracture structure parameters are calculated, as shown in Table 4. The length, width, surface area, volume, and shape factor are selected as comparative indicators to describe the differences in the microstructure of various samples. It can be found that the average length, width, surface area, volume, and shape factor of sample X3-T-2 are all greater than those of sample X3-B-1, with times of 1.070, 1.065, 1.143, 1.429, and 1.083. This indicates that sample X3-T-2 has larger, more complex and numerous pores and fractures compared to sample X3-B-1, which will result in their distinct seepage behaviors and different permeabilities.

On the basis of the Navier-Stokes equations and the fluid continuity equation, the microscopic dynamic seepage processes of representative elementary volumes (REVs) of sample X3-B-1 and sample X3-T-2 are simulated (Fig. 12) to analyze the differences in heterogeneous seepage. Obviously, not all pores and fractures have equal fluid distribution in them. The seepage dead zones (blue areas) in sample X3-B-1 are scattered throughout the entire seepage domain, obstructing the fluid flow process. In contrast, the seepage dead zones in sample X3-T-2 are mainly distributed in localized areas at the bottom and disappear completely as time progresses. This indicates that there are more unobstructed seepage channels

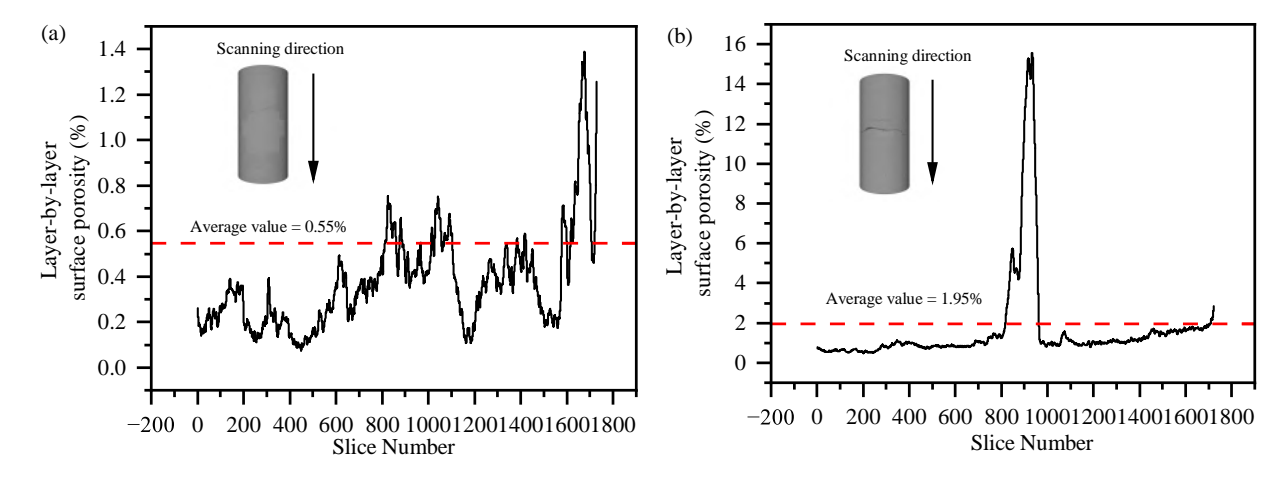


Fig. 11. Layer-by-layer surface porosity analysis of samples: (a) X3-B-1 and (b) X3-T-2.

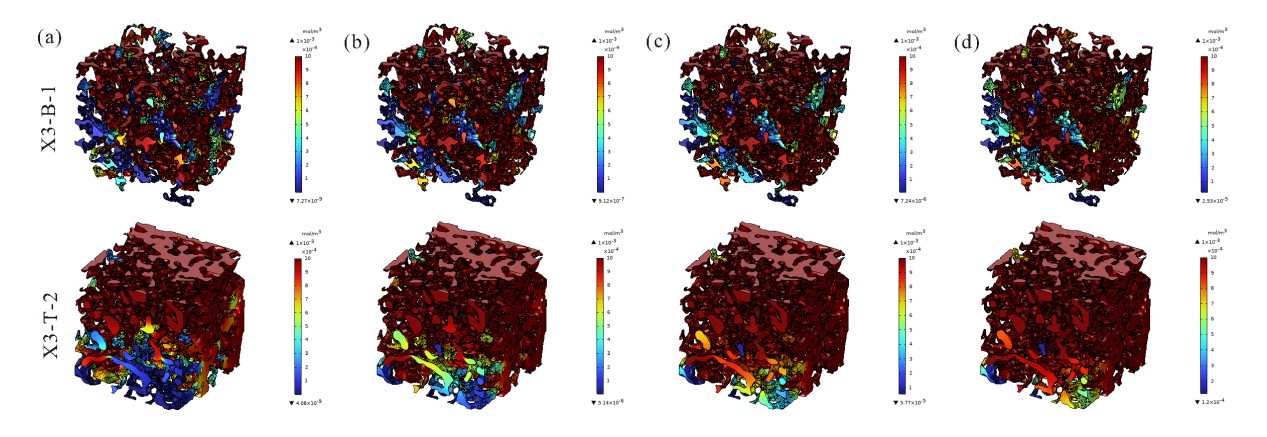


Fig. 12. Fluid mass distribution of REVs in different samples: (a) 1.25 s, (b) 2.5 s, (c) 3.75 s and (d) 5 s.

inside this sample, which facilitates the rapid migration of fluid.

In order to quantitatively compare the differences in permeability obtained from numerical simulations and model tests, the numerically simulated permeabilities of Sample X3-B-1 and Sample X3-T-2 are calculated based on Darcy's law, which are 3.726 and 15.175 mD, respectively. Compared with those of model A and model B (4.254 and 17.975 mD), the errors are 12.41% and 15.58%. Considering the dimensional differences between the model test and the numerical simulation, these errors are within an acceptable range. Therefore, the microscopic seepage numerical simulations of REVs not only verify the rationality of permeability testing via model experiments but also demonstrate the seepage heterogeneity and permeability anisotropy characteristics of uranium-bearing sandstone.

### 4.3 Discussion of the permeability testing results

#### 4.3.1 Influence of the stacking structure of model materials

One of the main formation models of sandstone-type uranium deposits in northern China is the interstratal oxidation zone type (Wang et al., 2025). Restricted by the influence of the sedimentary process, the internal particles of uranium deposits have complex shapes and diverse stacking modes (Wang et al., 2022b; Hu et al., 2024; Niu et al., 2025), which exert

a significant controlling effect on the permeability of uranium ore layers. The permeability difference between the two prepared models in this work also reflects this phenomenon and simultaneously reveals a relatively interesting mechanism of permeability control by microstructure. The influence of grade on the permeability of different models is shown in Fig. 13. Compared with model B, a certain amount of gravel is added to model A, which is mixed in the concrete and distributed randomly in space, resulting in the model presenting a basal cementation mode. The water in concrete mainly flows through pores, which are relatively stable. The gravel is denser and has lower permeability, and its presence makes the seepage of water more disordered (Zhou et al., 2021). In particular, there is often a flow-around phenomenon around the gravel, which makes the flow lines more tortuous and inhibits the seepage capacity of the model specimen. On the contrary, the water in model B mainly adopts a nearly uniform seepage mode and the formed flow lines are smoother, which makes the seepage process of water more unobstructed, resulting in its relatively high permeability. This is precisely because the composition of sandstone-type uranium deposits is so extremely complex that the *in-situ* permeability testing of uranium ore layers becomes more important, with greater difficulty and higher requirements.

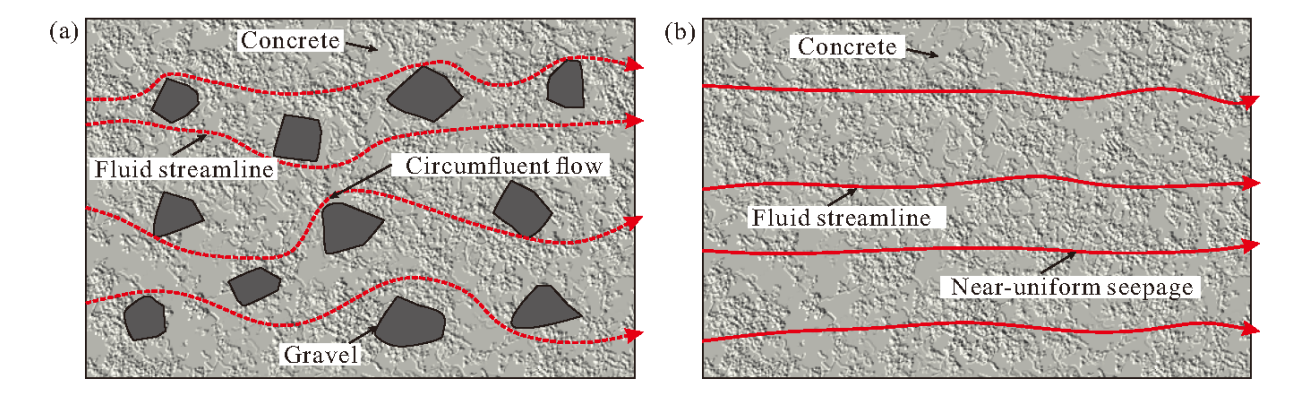


Fig. 13. Influence of grade on the permeability of different models: (a) Model A and (b) model B.

## **4.3.2** On-site application analysis of the permeability testing system

Although the model tests in this work have confirmed that the proposed permeability testing system is feasible and can be further promoted to field applications, the permeability testing system still has some potential errors due to the large burial depth of uranium ore layers and the complex structure of wellbores. These errors are closely related to the testing system and the testing process. In terms of the testing system, the high-pressure water storage tank and water delivery cable may undergo deformation and friction under the action of pulse pressure, leading to changes in the pulse pressure wave input to the target uranium deposit layer. In addition, there may be a risk of leakage at the joints between the four major parts of the testing system under long-term action, which can result in inaccurate pulse pressure attenuation curves. Meanwhile, the sensors used may have inherent errors that may reduce the accuracy of test results. In terms of the testing process, local damage to the wellbore casing or wellbore wall may lead to poor sealing of the measurement section system, and the accurate installation of the measurement section system in the target layer of the uranium deposit to be tested is also a key factor affecting the permeability evaluation results. Therefore, future research should focus on the key technical links in the application of the permeability testing system for deep uranium deposits, build a set of application technologies, and realize the in-situ, rapid and accurate evaluation of lowpermeability sandstone-type uranium deposits.

#### 5. Conclusions

- 1) An in-situ permeability testing system based on the pressure pulse method for low-permeability sandstone-type uranium deposits has been developed in this work, which consists of a pulse pressure application system, a control and monitoring system, a fixing and sealing system, and a measuring section system. By monitoring the time-dependent attenuation curve of the injected pulse pressure in real time, this system can automatically calculate the in-situ permeability and rapidly and accurately evaluate the penetration capability of specific horizons in low-permeability sandstone-type uranium deposits.
- 2) Two model blocks with dimensions of 1 m  $\times$  1 m  $\times$

- 2 m were prepared using cement, sand and gravel as materials in this work, and model tests for permeability measurement were conducted. The permeability of model A and model B ranged from 2.655 to 6.080 mD and from 14.904 to 22.080 mD, respectively, and both showed an exponential function relationship with pulse pressure. The model test results were basically consistent with the laboratory results and micro-seepage numerical simulation results of uranium deposit cores in terms of order of magnitude and law, but the permeability values from the model tests were higher (with errors of 7.14%-21.47%). This is related to factors such as the model tests not considering confining pressure, the uneven pouring of model blocks, and the local cracking of model specimens caused by pulse pressure.
- The permeability test results are related to the mineral stacking structure, testing system, and testing technology. Uranium deposit layers that contain gravel locally and are mainly dominated by basal cementation have more complex seepage paths and relatively lower permeability. In the testing system, the deformation and friction of the high-pressure water storage tank and cable, as well as the loose connections between various components, may reduce the accuracy of permeability testing. In addition, the integrity of the wellbore casing or wellbore wall and the installation position of the measuring section system are also major factors affecting the permeability test results. The next step will be to optimize the testing technology based on field tests, so as to establish a rapid and accurate in-situ technology for testing the permeability of lowpermeability sandstone-type uranium deposits.

#### Acknowledgements

This study was funded by the National Natural Science Foundation of China (No. 12372375), the Hebei Natural Science Foundation (Nos. A2024210057 and E2025210180) and the Science Research Project of Hebei Education Department (No. BJ2025094).

#### **Conflict of interest**

The authors declare no competing interest.

Open Access This article is distributed under the terms and conditions of the Creative Commons Attribution (CC BY-NC-ND) license, which permits unrestricted use, distribution, and reproduction in any medium, provided the original work is properly cited.

#### References

- Abzalov, M. Z. Sandstone-hosted uranium deposits amenable for exploitation by *in situ* leaching technologies. Applied Earth Science, 2012, 121(2): 55-64.
- Akhtar, S., Yang, X., Pirajno, F. Sandstone type uranium deposits in the Ordos basin, northwest china: A case study and an overview. Journal of Asian Earth Sciences, 2017, 146: 367-382.
- Al-Wardy, W., Zimmerman, R. W. Effective stress law for the permeability of clay-rich sandstones. Journal of Geophysical Research: Solid Earth, 2004, 109(B4): 04203.
- Bauer, C., Homand, F., Henry, J. P. *In situ* low permeability pulse test measurements. International Journal of Rock Mechanics and Mining Sciences & Geomechanics Abstracts, 1995, 32(4): 357-363.
- Bernabe, Y., Brace, W. F., Evans, B. Permeability, porosity and pore geometry of hot-pressed calcite. Mechanics of Materials, 1982, 1(3): 173-183.
- Bernabé, Y., Mok, U., Evans, B. A note on the oscillating flow method for measuring rock permeability. International Journal of Rock Mechanics and Mining Sciences, 2006, 43(2): 311-316.
- Biot, M. A. General theory of three-dimensional consolidation. Journal of Applied Physics, 1941, 12(2): 155-164.
- Bowell, R. J., Grogan, J., Hutton-Ashkenny, M., et al. Geometallurgy of uranium deposits. Minerals Engineering, 2011, 24(12): 1305-1313.
- Bredehoeft, J. D., Papadopulos, S. S. A method for determining the hydraulic properties of tight formations. Water Resources Research, 1980, 16(1): 233-238.
- Butler Jr, J. J. Pumping tests in nonuniform aquifers-the radially symmetric case. Journal of Hydrology, 1988, 101(1-4): 15-30.
- Cao, C. Transient surface permeability test: Experimental results and numerical interpretation. Construction and Building Materials, 2017, 138: 496-507.
- Chen, Q., Qi, Y., Mao, J., et al. Permeability test of granite mass by using pressure pulse test method. Rock and Soil Mechanics, 2005, 26(9): 1469-1472. (in Chinese)
- Chen, S., Xing, W., Du, X. Forecast of the demand and supply plan of China's uranium resources till 2030. International Journal of Green Energy, 2017, 14(7): 638-649.
- Chi, P., Sun, J., Zhang, R., et al. Multidimensional data-driven porous media reconstruction: Inversion from 1D/2D pore parameters to 3D real pores. Petroleum Science, 2025, 22(7): 2777-2793.
- Cooper Jr, H. H., Bredehoeft, J. D., Papadopulos, I. S. Response of a finite-diameter well to an instantaneous charge of water. Water Resources Research, 1967, 3(1): 263-269.
- Cosenza, P., Ghoreychi, M., Bazargan-Sabet, B., et al. *In situ* rock salt permeability measurement for long term safety assessment of storage. International Journal of

- Rock Mechanics and Mining Sciences, 1999, 36(4): 509-526.
- Cui, X., Bustin, A., Bustin, R. M. Measurements of gas permeability and diffusivity of tight reservoir rocks: Different approaches and their applications. Geofluids, 2009, 9(3): 208-223.
- David, C., Wong, T. F., Zhu, W., et al. Laboratory measurement of compaction-induced permeability change in porous rocks: Implications for the generation and maintenance of pore pressure excess in the crust. Pure and Applied Geophysics, 1994, 143(1): 425-456.
- Dong, S., Xu, L., Dai, Z., et al. A novel fractal model for estimating permeability in low-permeable sandstone reservoirs. Fractals-Complex Geometry Patterns and Scaling in Nature and Society, 2020, 28(8): 2040005.
- Egermann, P., Lenormand, R., Longeron, D., et al. A fast and direct method of permeability measurements on drill cuttings. SPE Reservoir Evaluation & Engineering, 2005, 8(4): 269-275.
- Elkatatny, S., Mahmoud, M., Tariq, Z., et al. New insights into the prediction of heterogeneous carbonate reservoir permeability from well logs using artificial intelligence network. Neural Computing & Applications, 2018, 30(9): 2673-2683.
- Fang, J., Lau, C. K. M., Lu, Z., et al. Estimating peak uranium production in china – based on a stella model. Energy Policy, 2018, 120: 250-258.
- Fisher, Q., Lorinczi, P., Grattoni, C., et al. Laboratory characterization of the porosity and permeability of gas shales using the crushed shale method: Insights from experiments and numerical modelling. Marine and Petroleum Geology, 2017, 86: 95-110.
- Gao, Q., Yu, X. An innovative Time Domain Reflectometry (TDR) sensor to monitor earthquake induced void redistribution in layered soils. Intelligent Geoengineering, 2024, 1(1): 78-87.
- Gao, Z., Hu, Q. Estimating permeability using median porethroat radius obtained from mercury intrusion porosimetry. Journal of Geophysics and Engineering, 2013, 10(2): 025014.
- Giot, R., Auvray, C., Conil, N., et al. Multi-stage water permeability measurements on claystone by steady and transient flow methods. Engineering Geology, 2018, 247: 27-37.
- Hasanov, A. K., Dugan, B., Batzle, M. L. Numerical simulation of oscillating pore pressure experiments and inversion for permeability. Water Resources Research, 2020, 56(6): e2019WR025681.
- Hu, M., Niu, Q., Yuan, W., et al. Evolution characteristic and mechanism of microstructure, hydraulic and mechanical behaviors of sandstone treated by acid-rock reaction: Application of *in-situ* leaching of uranium deposits. Journal of Hydrology, 2024, 643: 131948.
- Huang, Y., Shi, Z., Li, J., et al. Quantifying the mechanical properties of coal matrix and cleat using digital image correlation method. Deep Resources Engineering, 2025, 2(1): 100168.
- Iturrarán-Viveros, U., Parra, J. O. Artificial neural networks

- applied to estimate permeability, porosity and intrinsic attenuation using seismic attributes and well-log data. Journal of Applied Geophysics, 2014, 107: 45-54.
- Jacob, A., Peltz, M., Hale, S., et al. Simulating permeability reduction by clay mineral nanopores in a tight sandstone by combining computer X-ray microtomography and focussed ion beam scanning electron microscopy imaging. Solid Earth, 2021, 12(1): 1-14.
- Jiang, K., Zhou, W., Jia, N., et al. Analytical model of shale gas permeability based on the pore size distribution from FE-SEM and image analysis. Arabian Journal for Science and Engineering, 2024, 49(6): 8661-8677.
- Johnson, C. R., Greenkorn, R. A., Woods, E. G. Pulse-testing: A new method for describing reservoir flow properties between wells. Journal of Petroleum Technology, 1966, 18(12): 1599-1604.
- Katsube, T. J., Hume, J. P. Permeability determination in crystalline rocks by standard geophysical logs. Geophysics, 1987, 52(3): 342-352.
- Kim, H., Lettry, Y., Park, D., et al. Field evaluation of permeability of concrete linings and rock masses around underground lined rock caverns by a novel *in-situ* measurement system. Engineering Geology, 2012, 137-138: 97-106.
- Kozhevnikov, E., Turbakov, M., Riabokon, E., et al. Rock permeability evolution during cyclic loading and colloid migration after saturation and drying. Advances in Geo-Energy Research, 2024, 11(3): 208-219.
- Kranz, R. L., Saltzman, J. S., Blacic, J. D. Hydraulic diffusivity measurements on laboratory rock samples using an oscillating pore pressure method. International Journal of Rock Mechanics and Mining Sciences & Geomechanics Abstracts, 1990, 27(5): 345-352.
- Leven, C., Dietrich, P. What information can we get from pumping tests? Comparing pumping test configurations using sensitivity coefficients. Journal of Hydrology, 2006, 319(1-4): 199-215.
- Li, G., Yao, J. A review of *in situ* leaching (ISL) for uranium mining. Mining, 2024, 4(1): 120-148.
- Li, J., Liu, D., Yao, Y., et al. Evaluation of the reservoir permeability of anthracite coals by geophysical logging data. International Journal of Coal Geology, 2011, 87(2): 121-127.
- Li, K., Li, H., Khudhair, A., et al. Efficient generation of digital rock CT images using LoRA-enhanced stable diffusion models. Intelligent Geoengineering, 2025, 2(2): 96-108.
- Li, K., Wang, W., Yang, D., et al. Application of periodic oscillation method in low permeability measurement. Rock and Soil Mechanics, 2020, 41(3): 1086-2094. (in Chinese)
- Ling, K., He, J., Pei, P., et al. Determining the permeability of tight rock with gas transient flow. Journal of Natural Gas Science and Engineering, 2013, 15: 1-7.
- Liu, Q., Lv, B., Konietzky, H., et al. A novel method for rock permeability determination based on the pressure pulse decay method and inverse numerical simulations. Rock Mechanics and Rock Engineering, 2024a, 57(12): 10229-

- 10244.
- Liu, Y., He, Y., Chen, J., et al. Progress on enhancing seepage-leaching mass-transfer research for *in-situ* leaching mining of low-permeability uranium-bearing sandstone: A review. Journal of Radioanalytical and Nuclear Chemistry, 2024b, 333(9): 4485-4502.
- Long, H., Zhou, X., He, Y., et al. Artificial intelligence seismic permeability prediction method based on highdimensional petrophysical template. Applied Geophysics, 2025, 22(2): 397-407.
- Mansur, C. I., Dietrich, R. J. Pumping test to determine permeability ratio. Journal of the Soil Mechanics and Foundations Division, 1965, 91(4): 151-183.
- Marsala, A. F., Figoni, A., Brignoli, M. Transient method implemented under unsteady-state conditions for low and very low permeability measurements on cuttings. Paper SPE 47202 Presented at SPE Annual Technical Conference and Exhibition, SPE/ISRM Rock Mechanics in Petroleum Engineering, Rondheim, Norway, 8-10 July, 1998.
- Meng, Z., Zhang, J., Wang, R. *In-situ* stress, pore pressure and stress-dependent permeability in the southern qinshui basin. International Journal of Rock Mechanics and Mining Sciences, 2011, 48(1): 122-131.
- Metwally, Y. M., Sondergeld, C. H. Measuring low permeabilities of gas-sands and shales using a pressure transmission technique. International Journal of Rock Mechanics and Mining Sciences, 2011, 48(7): 1135-1144.
- Mukherjee, S., Goswami, S., Zakaulla, S. Geological relationship between hydrocarbon and uranium: Review on two different sources of energy and the indian scenario. Geoenergy Science and Engineering, 2023, 221: 111255.
- Ni, H., Liu, J., Huang, B., et al. Quantitative analysis of pore structure and permeability characteristics of sandstone using SEM and CT images. Journal of Natural Gas Science and Engineering, 2021, 88: 103861.
- Niu, Q., Cao, L., Sang, S., et al. Experimental study on the softening effect and mechanism of anthracite with CO<sub>2</sub> injection. International Journal of Rock Mechanics and Mining Sciences, 2021, 138: 104614.
- Niu, Q., Hu, M., Chang, J., et al. Explosive fracturing mechanism in low-permeability sandstone-type uranium deposits considering different acidification reactions. Energy, 2024a, 312: 133676.
- Niu, Q., Wang, J., He, J., et al. Evolution of pore structure, fracture morphology and permeability during CO<sub>2</sub>+O<sub>2</sub> *in-situ* leaching process of fractured sandstone. Energy, 2025, 315: 134348.
- Niu, Q., Wang, X., Chang, J., et al. Influencing mechanisms of multi-scale pore-fracture responses of coals on their macro/micromechanical behaviors under ScCO<sub>2</sub> injection. Advances in Geo-Energy Research, 2024b, 14(1): 64-80.
- Peyraube, N., Villanueva, J. D., Lastennet, R., et al. Assessing the dispersion of hydraulic conductivity values estimated using the dupuit, thiem, and boulton methods on repeated pumping tests in an unconfined aquifer. Hydrogeology Journal, 2023, 31(7): 1863-1882.

- Ren, J., Niu, Q., Wang, Z., et al. CO<sub>2</sub> adsorption/desorption, induced deformation behavior, and permeability characteristics of different rank coals: Application for CO<sub>2</sub>-enhanced coalbed methane recovery. Energy & Fuels, 2022, 36(11): 5709-5722.
- Schembre, J. M., Kovscek, A. R. A technique for measuring two-phase relative permeability in porous media via X-ray CT measurements. Journal of Petroleum Science and Engineering, 2003, 39(1-2): 159-174.
- Selvadurai, A., Boulon, M. J., Nguyen, T. S. The permeability of an intact granite. Pure and Applied Geophysics, 2005, 162(2): 373-407.
- Shannak, S. D., Cochrane, L., Bobarykina, D. Global uranium market dynamics: Analysis and future implications. International Journal of Sustainable Energy, 2025, 44(1): 2457376.
- Stormont, J. C. Conduct and interpretation of gas permeability measurements in rock salt. International Journal of Rock Mechanics and Mining Sciences, 1997, 34(3-4): 301-303.
- Su, X., Liu, Z., Yao, Y., et al. Petrology, mineralogy, and ore leaching of sandstone-hosted uranium deposits in the ordos basin, north China. Ore Geology Reviews, 2020, 127: 103768.
- Tang, X., Cheng, C.. Fast inversion of formation permeability from stoneley wave logs using a simplified biotrosenbaum model. Geophysics, 1996, 61(3): 639-645.
- Vemuri, V., Dracup, J. A. Analysis of nonlinearities in ground water hydrology: A hybrid computer approach. Water Resources Research, 1967, 3(4): 1047-1058.
- Wang, B., Yue, L., Liu, J., et al. Ion migration in *in-situ* leaching (ISL) of uranium: Field trial and reactive transport modelling. Journal of Hydrology, 2022a, 615: 128634.
- Wang, Q., Liang, X., Wang, W., et al. Mineral composition and full-scale pore structure of qianjiadian sandstone-type uranium deposits: Application for *in situ* leaching mining. Geofluids, 2022b, 2022: 2860737.

- Wang, Q., Peng, H., Liu, C., et al. Constraints of reducing media on uranium mineralization in the uranium-bearing rock systems of the southern Songliao basin. Ore Geology Reviews, 2025, 176: 106406.
- Wang, W., Liang, X., Niu, Q., et al. Reformability evaluation of blasting-enhanced permeability in *in situ* leaching mining of low-permeability sandstone-type uranium deposits. Nuclear Engineering and Technology, 2023, 55(8): 2773-2784.
- Wang, X., Ge, H., Chen, H. Ultralow permeability measurements with periodic oscillation method. Rock and Soil Mechanics, 2015, 36(S2): 237-244. (in Chinese)
- Zhao, J., Kang, Z. Permeability of oil shale under *in situ* conditions: Fushun oil shale (China) experimental case study. Natural Resources Research, 2021, 30(1): 753-763.
- Zhao, Y., Wang, C., Bi, J. A method for simultaneously determining axial permeability and transverse permeability of tight reservoir cores by canister degassing test. Energy Science & Engineering, 2020, 8(4): 1220-1230.
- Zhou, X., Sang, S., Niu, Q., et al. Changes of multiscale surface morphology and pore structure of mudstone associated with supercritical CO<sub>2</sub>-water exposure at different times. Energy & Fuels, 2021, 35(5): 4212-4223.
- Zhou, X., Wang, W., Niu, Q., et al. Geochemical reactions altering the mineralogical and multiscale pore characteristics of uranium-bearing reservoirs during CO<sub>2</sub>+O<sub>2</sub> in situ leaching. Frontiers in Earth Science, 2023, 10: 1094880.
- Zhou, Y., Wu, S., Zhu, R., et al. A new model for determining the effective permeability of tight reservoirs based on Fractal-Monte Carlo method. Petroleum Science, 2025, 22(8): 3101-3118.
- Zhu, H., Ju, Y., Lu, Y., et al. Natural evidence of organic nanostructure transformation of shale during bedding-parallel slip. Geological Society of America Bulletin, 2025, 137(5-6): 2719-2746.